

ARTICLE

Open Access

# Bowing-alleviated continuous bandgap engineering of wafer-scale $WS_{2x}Se_{2(1-x)}$ monolayer alloys and their assembly into hetero-multilayers

Hee Seong Kang<sup>1</sup>, Jung Hoon Kang<sup>1</sup>, Sol Lee<sup>2</sup>, Kihyun Lee<sup>2</sup>, Do Hyoung Koo<sup>1</sup>, Yong-Sung Kim<sup>3</sup>, Young Joon Hong<sup>4</sup>, Yong-Jin Kim<sup>5</sup>, Kwanpyo Kim<sup>2</sup>, Donghun Lee<sup>1</sup> and Chul-Ho Lee<sup>1,6,7</sup>

## Abstract

Bandgap engineering of compound semiconductors and the fabrication of bandgap-modulated heterostructures are important for enabling the development of modern optoelectronics. However, these engineering processes are challenging for two-dimensional (2D) semiconductors of transition metal dichalcogenides, particularly on a large scale. Herein, we report the wafer-scale homogeneous growth of composition-modulated  $WS_{2x}Se_{2(1-x)}$  alloys with a continuously tunable bandgap using metal–organic chemical vapor deposition. Well-optimized growth produces monolayer films with excellent homogeneity over the entire wafer. The substitutional atomic chalcogen (S, Se) concentration in  $WS_{2x}Se_{2(1-x)}$  alloys is precisely controlled by varying the flow rate of the metal–organic precursors, leading to a bandgap modulation from 1.67 to 2.05 eV, as determined from absorbance spectra. Notably, the optical bandgap of  $WS_{2x}Se_{2(1-x)}$  alloys exhibits a nearly linear relationship with the chalcogen composition, implying a low bowing effect. This bowing-alleviated bandgap modulation is attributed to the small lattice mismatch, strain relaxation, and thermodynamic miscibility in the  $WS_{2x}Se_{2(1-x)}$  alloys, as confirmed by density-functional theory calculations. Furthermore, the fabrication of hetero-multilayers by stacking differently alloyed films is demonstrated. The produced heterostructure film exhibits a broad spectral absorbance distinct from that of the individual layers. The findings of this study provide insights for the advancement of versatile design of functional 2D optoelectronics.

## Introduction

As atomically thin-layered semiconductors, two-dimensional (2D) transition metal dichalcogenides (TMDs) have recently attracted significant scientific and industrial interest owing to their exceptional optical, electrical, and mechanical properties<sup>1–3</sup>. In particular, their strong light–matter interactions and large exciton binding energy at the 2D limit have made them promising material candidates for flexible, transparent, and heterogeneously integrated optoelectronic devices such as

photodetectors, image sensors, solar cells, and light-emitting devices. The most commonly investigated group-VI TMDs ( $MX_2$ ,  $M = Mo \text{ \& \ } W$ , and  $X = S \text{ \& \ } Se$ ) have a wide bandgap energy range (1.6–2.0 eV), as the precise control of their bandgap energy is necessary for the design versatility of 2D TMD-based optoelectronic devices<sup>3–5</sup>. In this context, various strategies for the bandgap engineering of semiconducting TMDs have been reported, including layer number control, heterostructure formation, strain engineering, and alloying<sup>6–11</sup>. Among these, chemical alloying based on composition modulation offers better thermodynamic control and stability and is thus an effective approach for achieving continuous and systematic bandgap engineering<sup>10,12</sup>.

In conventional III-V compound semiconductors, alloying-based bandgap engineering has been widely

Correspondence: Donghun Lee (dh0102.lee@gmail.com)

Chul-Ho Lee (chulholee@gmail.com)

<sup>1</sup>KU-KIST Graduate School of Converging Science and Technology, Korea University, Seoul 02841, Republic of Korea

<sup>2</sup>Department of Physics, Yonsei University, Seoul 03722, Republic of Korea

Full list of author information is available at the end of the article

© The Author(s) 2022



**Open Access** This article is licensed under a Creative Commons Attribution 4.0 International License, which permits use, sharing, adaptation, distribution and reproduction in any medium or format, as long as you give appropriate credit to the original author(s) and the source, provide a link to the Creative Commons license, and indicate if changes were made. The images or other third party material in this article are included in the article's Creative Commons license, unless indicated otherwise in a credit line to the material. If material is not included in the article's Creative Commons license and your intended use is not permitted by statutory regulation or exceeds the permitted use, you will need to obtain permission directly from the copyright holder. To view a copy of this license, visit <http://creativecommons.org/licenses/by/4.0/>.

employed to control the optical properties and band structure of heteroepitaxial thin films, thereby enabling various optoelectronic devices, such as solar cells, light-emitting diodes, and lasers<sup>13–17</sup>. However, bandgap tunability has been limited due to the solubility limit and miscibility gap in alloy compounds and the formation of dislocations and precipitates during heteroepitaxy<sup>18</sup>. In contrast, TMD-based alloy films, which have continuously tunable bandgap energy, can be easily formed by controlling their substitutional composition owing to their small lattice mismatch (~1%), strain relaxation by layered structure, and thermodynamic miscibility<sup>13</sup>. Recently, diverse synthetic methods based on two-step chemical vapor deposition (CVD) processes involving the chalcogenization (sulfurization and selenization) of predeposited transition metals (Mo and W), transition metal oxides, and solution precursors have been used to realize large-scale 2D TMD alloy films<sup>19–21</sup>. Although these two-step processes provide large-scale uniform TMD alloy films (such as  $\text{Mo}_{1-x}\text{W}_x\text{S}_2$  and  $\text{MoS}_{2(1-x)}\text{Se}_{2x}$ ), there remain problems arising from the difficulties of fine-tuning the composition and complexity of the growth processes. In addition, metal–organic chemical vapor deposition (MOCVD), a progressive CVD process, has been industrially proven to be powerful for the atomic-scale precision engineering of alloys and high crystalline growth of thin films since it offers fine control of the flow rate and surface reactions of the vapor-phase precursors<sup>22–25</sup>.

Herein, we report a one-step growth and in situ alloying methods to produce a wafer-scale  $\text{WS}_{2x}\text{Se}_{2(1-x)}$  monolayer with spatial homogeneity over the entire film using vertical MOCVD with multiple vapor-phase precursors. Fine-tuning the molar flow rates of sulfur and selenium precursors during growth allowed the full-range composition tunability of  $\text{WS}_{2x}\text{Se}_{2(1-x)}$  alloys, wherein  $x$  varied between 0 and 1. Notably, this enabled the linear modulation of the bandgap energy of the alloyed films with a low bowing effect. Furthermore, hetero-multilayer films comprising differently alloyed  $\text{WS}_{2x}\text{Se}_{2(1-x)}$  monolayers fabricated by artificial *van der Waals* (*vdW*) stacking exhibited broad spectral absorption with multiple exciton resonances.

## Materials and methods

### Wafer-scale growth of monolayer $\text{WS}_{2x}\text{Se}_{2(1-x)}$

The monolayer  $\text{WS}_{2x}\text{Se}_{2(1-x)}$  alloying films were directly grown on a 2-inch  $\text{SiO}_2$  (285 nm)/Si substrate in a home-built MOCVD with a vertical cold-wall chamber and independent gas pipeline manifold. Tungsten hexacarbonyl (THC,  $\text{W}(\text{CO})_6$ ), diethyl sulfide (DES,  $(\text{C}_2\text{H}_5)_2\text{S}$ ), and diethyl selenide (DESe,  $(\text{C}_2\text{H}_5)_2\text{Se}$ ) stored in stainless bubblers were used as metal–organic precursors for the transition metal and chalcogens, respectively. The 2-inch  $\text{SiO}_2$ /Si substrate was loaded onto the

graphite susceptor in the vertical reactor, heated to 600 °C at 45 °C  $\text{min}^{-1}$ , and post-annealed for surface cleaning. After reaching the growth temperature, the gaseous THC, DES, and DESe precursors were injected into the MOCVD reactor in 500 sccm Ar (99.999%) and 5 sccm  $\text{H}_2$  (99.999%). The total growth time and reactor pressure were 130 min and 50 Torr, respectively. In the MOCVD process, the molar flow rate of THC was fixed at  $8.35 \times 10^{-14}$  mole  $\text{min}^{-1}$ , but the molar flow rates of DES and DESe were systematically and independently controlled by changing the vapor pressure, line pressure, and carrier gas (Ar, 99.999%) flows for the growth of the  $\text{WS}_{2x}\text{Se}_{2(1-x)}$  alloying films with tunable bandgaps. After the growth process, the  $\text{WS}_{2x}\text{Se}_{2(1-x)}$  films were naturally cooled to room temperature and then unloaded from the reaction chamber.

### Optical characterization of monolayer $\text{WS}_{2x}\text{Se}_{2(1-x)}$ alloys

A homemade optical spectrometer combined with a 532-nm continuous laser and monochromator (Andor, 303i) was utilized to measure the PL and Raman spectra of the monolayer  $\text{WS}_{2x}\text{Se}_{2(1-x)}$  alloys under ambient conditions. The irradiated laser power and time were 120  $\mu\text{W}$  and 5 s, respectively. The PL and Raman signals were collected on an objective lens ( $\times 100$  magnification, N. A. = 0.9). The absorption spectra of the monolayer  $\text{WS}_{2x}\text{Se}_{2(1-x)}$  alloying films, which were transferred onto double-sided polished transparent c-sapphire substrates by the dry-transfer method, were measured using a UV-visible spectrophotometer (Agilent, 8453E) with a spectral range of 190–1100 nm. The spatially resolved PL and Raman mapping, sized  $50 \times 50 \mu\text{m}^2$ , were obtained on the X and Y axes by scanning the films on a motorized stage (in an optical spectrometer).

### Material characterization

AFM (Park systems, NX-10) and XPS (ULVAC-PHI, X-Tool) were employed to characterize and analyze the monolayer  $\text{WS}_{2x}\text{Se}_{2(1-x)}$  alloying films. A double Cs-corrected TEM (JEOL, JEM-ARM200F, 80 kV operation) was used for ADF-STEM imaging and EDX analysis. For ADF-STEM imaging, a convergence semiangle of 25 mrad and an ADF detector angle range of 80–160 mrad were used.

### Monte-Carlo simulation

The Monte-Carlo simulations were performed with Python-based codes. The atomic sites of Se + Se, Se + S, and S + S locations were selected randomly with given relative populations. Supplementary Fig. S6a shows a representative result with relative populations of 25% (Se + Se), 55% (Se + S), and 20% (S + S). They are represented by a Voronoi diagram. The codes used for the data are available from the corresponding authors upon reasonable request.

### Density functional theory calculations

DFT calculations were performed as implemented in the Vienna ab initio simulation package (VASP) code<sup>26</sup>. Projector-augmented wave (PAW) pseudopotentials<sup>27,28</sup> and a kinetic energy cutoff of 500 eV were applied. The Perdew, Burke, and Ernzerhof (PBE) functional within the generalized gradient approximation (GGA) was used for the exchange-correlation functional<sup>29</sup>, and the vdW-D2 correction proposed by Grimme was used to describe the long-range van der Waals interaction<sup>30,31</sup>. The monolayer  $WS_{2x}Se_{2(1-x)}$  alloy configurations were generated in a  $3 \times 3 \times 1$  monolayer  $WSe_2$  supercell by substituting S atoms with Se. Up to ten random alloy configurations were considered. A vacuum layer thickness of 6.4 Å was used. A  $\Gamma$ -centered  $2 \times 2 \times 1$  k-point mesh in the  $3 \times 3 \times 1$  supercell was used for the Brillouin zone (BZ) summation. For the  $WS_{2x}Se_{2(1-x)}$  alloys, the hexagonal lattice constant was optimized by constraining the hexagonal lattice structure. The local atomic configurations were relaxed to less than 0.001 eV Å<sup>-1</sup> in the Hellmann–Feynman forces.

### Transfer and absorption measurements of mono-, bi-, and trilayer $WS_{2x}Se_{2(1-x)}$ alloys

To transfer the monolayer  $WS_{2x}Se_{2(1-x)}$  alloys onto the transparent substrate, we adopted the dry-transfer process method using a thermal release tape (TRT). First, PMMA 495 K (Micro Chem.) was spin-coated on the as-grown  $WS_{2x}Se_{2(1-x)}$  film on the  $SiO_2/Si$  substrate at 4000 rpm for 90 s. The coated PMMA was then baked at 180 °C for 10 min. TRT (Graphene Square, GA-TRT-01) was attached to the PMMA/ $WS_{2x}Se_{2(1-x)}$  film, and the resultant TRT/PMMA/ $WS_{2x}Se_{2(1-x)}$  was then mechanically peeled from the  $SiO_2/Si$  substrate. After separation, the TRT/PMMA/ $WS_{2x}Se_{2(1-x)}$  layer was stuck on the double-side polishing c-sapphire, which was employed as the transparent substrate and treated by O<sub>2</sub> plasma. The TRT was released by heating at 110 °C for 2 min on a hot plate. The PMMA was removed by dipping in acetone for 20 min, after which the sample was rinsed using IPA solution. For the fabrication of the stacked trilayer alloying film with varying chalcogen compositions, the same transfer method was repeated for the second and third films. Absorption measurements of the mono-, bi-, and trilayer alloying films were performed using a UV-vis–NIR spectrophotometer (Agilent, Cary 5000) with a spectral range of 175–3300 nm.

### Results and discussion

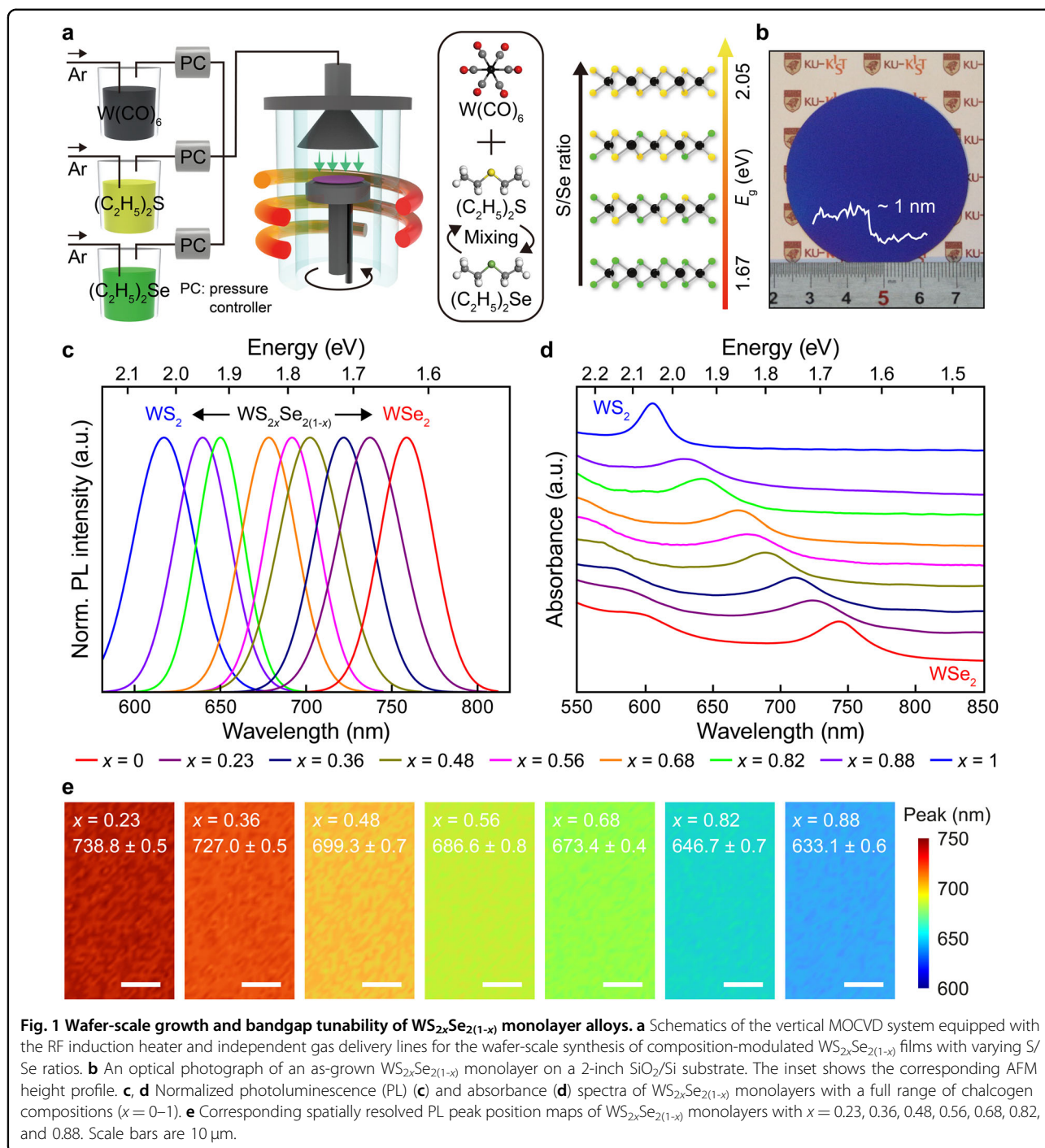
The uniform wafer-scale synthesis of  $WS_{2x}Se_{2(1-x)}$  alloys was achieved by using a vertical MOCVD system. Figure 1a represents the schematics of the vertical cold-wall MOCVD equipped with a radio frequency (RF) induction heater and independent gas line manifold for the wafer-scale synthesis of composition-modulated  $WS_{2x}Se_{2(1-x)}$

alloy films with varying chalcogen (S, Se) contents. For the composition-modulated growth of  $WS_{2x}Se_{2(1-x)}$  alloys with varying chalcogen composition ( $x = 0–1$ ), the chalcogen (S, Se) concentration was finely controlled by varying the molar flow rates of diethyl sulfide (DES, S precursor) and diethyl selenide (DESe, Se precursor) stored in stainless bubblers. The molar flow rates of DES and DESe were, in turn, independently controlled by varying the vapor pressure, line pressure, and carrier gas flow, while the molar flow rate of tungsten hexacarbonyl (WHC, W precursor) was fixed during the growth process. The detailed growth process is described in the Experimental Methods section.

Figure 1b shows a photograph of the as-grown monolayer  $WS_{2x}Se_{2(1-x)}$  alloy film fully covered on a 2-inch  $SiO_2/Si$  wafer. The representative  $WS_{2x}Se_{2(1-x)}$  film shows a uniform contrast on the entire substrate, indicating the homogeneity of the film. The atomic force microscope (AFM) measurement confirmed that the as-grown film exhibited a smooth surface and ~1 nm thickness, corresponding to that of monolayer TMDs (Supplementary Fig. S1).

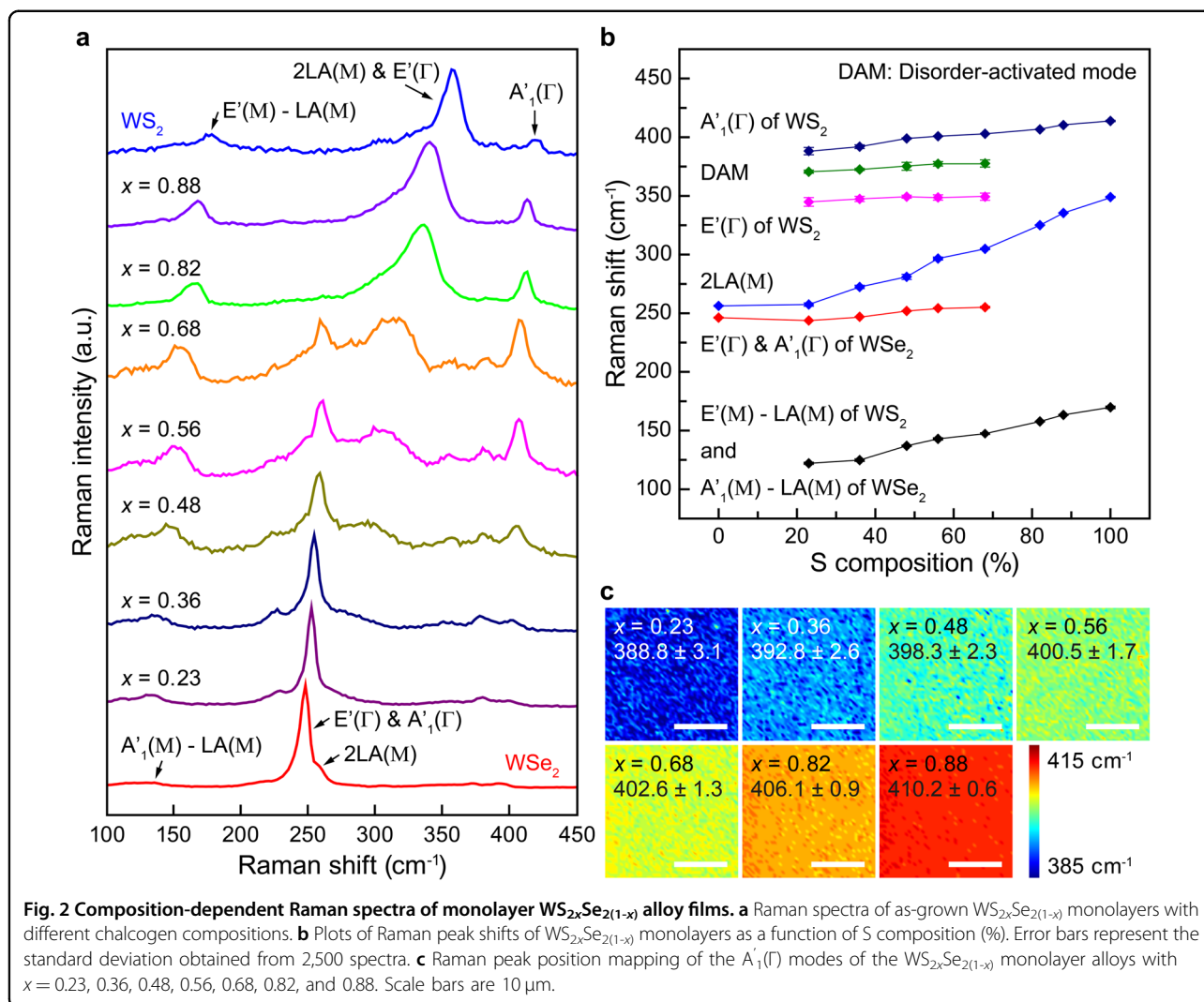
The controlled bandgap modulation of the  $WS_{2x}Se_{2(1-x)}$  alloys was confirmed by optical characterization techniques such as photoluminescence (PL) and absorption spectroscopy. As the sulfur content ( $x$ ) in the alloys increased from 0 to 1, the PL peak positions of the films continuously changed from 759 to 609 nm, corresponding to the bandgap energy of monolayers,  $WSe_2$  and  $WS_2$ , respectively. The PL spectra exhibited a strong single peak emission with a full-width at half maximum (FWHM) of ~33–46 nm (Fig. 1c and Supplementary Fig. S2). Similarly, the UV–visible absorbance spectra of  $WS_{2x}Se_{2(1-x)}$  alloys showed a tunable A exciton shift from 743 ( $WSe_2$ ) to 604 nm ( $WS_2$ ) with varying relative sulfur compositions (Fig. 1d and Supplementary Fig. S3), which is consistent with the previously reported values for pure monolayers  $WSe_2$  (729 nm) and  $WS_2$  (620 nm)<sup>32</sup>. In addition, the spatially resolved PL peak position mapping images of monolayer  $WS_{2x}Se_{2(1-x)}$  alloys with different chalcogen compositions showed high optical uniformity over the entire area (Fig. 1e). To further validate the wafer-scale uniformity of alloy films, PL and Raman spectra were obtained at different positions over the entire wafer (Supplementary Fig. S4). The PL peak positions of the  $WS_2$ ,  $WS_{0.82}Se_{1.18}$ , and  $WSe_2$  films are  $612.9 \pm 2.1$ ,  $718.6 \pm 1.6$ , and  $761.9 \pm 1.8$  nm, showing small variations of 1.1%, 0.8%, and 0.9% inhomogeneity ((max-min)/average), respectively. This further implies that the alloy films with composition-modulated bandgap energies had a homogeneous chalcogen composition throughout the entire wafer without any significant structural disorders or additional phases.

Furthermore, we investigated the influence of composition alloying upon substitution of chalcogen (S, Se) atoms on the lattice vibration behaviors of alloy



compounds via Raman measurements using a 532-nm laser as the excitation source (Fig. 2). The Raman spectra of all synthesized  $WS_{2x}Se_{2(1-x)}$  monolayers were dominated by four basic Raman modes:  $E'$  resulting from the in-plane displacement of S and Se atoms with respect to the W atoms,  $A_1'$  associated with the out-of-plane vibrations of S and Se atoms, longitudinal acoustic (LA) phonons involving the in-plane collective movements of

atoms, and the alloying mode combined with the sulfur and selenium atoms<sup>33,34</sup>. Varying the relative chalcogen compositions resulted in evolutionary peak shifts, and the corresponding extension and reduction of the lattice vibration modes for  $WS_{2x}Se_{2(1-x)}$  alloys were observed. In pure  $WSe_2$  ( $x = 0$ ), the main Raman peak was observed at  $248.2 \text{ cm}^{-1}$ , known as the superposition of the  $E'(\Gamma)$  and  $A_1'(\Gamma)$  modes. In addition, the  $354.9 \text{ cm}^{-1}$  ( $2LA(M) +$



$E'(\Gamma)$  and  $417 \text{ cm}^{-1}$  ( $A'_1(\Gamma)$ ) modes appeared mainly in pure  $WS_2$  ( $x = 1$ ). Upon alloying, the  $2LA(M)$  mode continuously shifted from  $258.8$  (pure  $WSe_2$ ) to  $352.9 \text{ cm}^{-1}$  (pure  $WS_2$ ), and we also observed newly evolved modes from  $380.3$  ( $WSe_2$ -rich phase) to  $384.5 \text{ cm}^{-1}$  ( $WS_2$ -rich phase) in the  $WS_{2x}Se_{2(1-x)}$  alloys, attributed to the disorder-activated peak<sup>34</sup>. In addition, the superposition of  $E'(M)$ - $LA(M)$  of  $WS_2$  and  $A'_1(M)$ - $LA(M)$  of  $WSe_2$  shifted from  $131.7$  to  $176.3 \text{ cm}^{-1}$  upon increasing the sulfur concentration in the  $WS_{2x}Se_{2(1-x)}$  alloys; separating the peak positions for the signals originating from each mode was difficult. The above-mentioned Raman peaks were gradually changed by tuning the chalcogen compositions, as shown in Fig. 2b and Supplementary Table S1. The systematic blueshifts in the Raman peaks could be attributed to the changed mass and distorted bond length upon substituting Se atoms in the  $WS_{2x}Se_{2(1-x)}$  lattice with S<sup>35,36</sup>. In addition, according to the Raman maps of the  $A'_1(\Gamma)$  peak position of

$WS_{2x}Se_{2(1-x)}$  with different sulfur compositions (Fig. 2c), the alloyed films exhibited small spatial fluctuations in the Raman peak position over the entire measured area. When  $x = 0.23$ , the largest standard deviation of  $3.1 \text{ cm}^{-1}$  corresponds to less than 1% of the average values of Raman peaks. Furthermore, to validate the wafer-scale uniformity, Raman spectra were obtained at different positions over the entire wafer (Supplementary Fig. S4). Both alloyed and non-alloyed films showed spatial homogeneity with similar spectra regardless of the measured position on the wafer. Particularly, for the  $WS_{0.82}Se_{1.18}$  film, the standard deviation of  $LA(M)$  modes was measured to be  $1.4 \text{ cm}^{-1}$ , which is only 0.5% of the average values. These results indicate the macroscopic uniformity of MOCVD-grown  $WS_{2x}Se_{2(1-x)}$  alloys.

The atomic-level substitution of the chalcogen atoms in the alloyed film was further confirmed by using annular dark-field scanning transmission electron microscopy (ADF-STEM). The high-resolution STEM image of

WS<sub>2x</sub>Se<sub>2(1-x)</sub> showed a hexagonal patterned arrangement of the atoms, similar to that in the monolayer TMDs. In addition, according to the false-color DF-TEM images (Supplementary Fig. S5), the alloyed WS<sub>0.82</sub>Se<sub>1.18</sub> and non-alloyed WS<sub>2</sub> films show similar average grain sizes of 41 ± 14 and 54 ± 26 nm, respectively, close to the grain sizes attained by previous studies for MOCVD-grown TMD monolayers (typically from a few tens of nanometers to a few micrometers)<sup>22,37</sup>. Each atom in the high-resolution STEM image could be distinguished by its brightness and contrast (Fig. 3a). The brightest spots in the image corresponded to the W atoms (solid orange circle) because the atomic number of W (74) is larger than that of S (16) and Se (34) atoms. The Se + Se atoms (solid green circle) were relatively brighter than the Se + S (sky blue solid circle) and S + S atoms (solid yellow circle). Their atomic configurations were distinct from each other in the atomic image (top of Fig. 3b) and line profile of ADF intensity (bottom of Fig. 3b). Based on the counted histogram of ADF intensities of all the elements in the ADF-STEM image, the S composition was determined to be 47.7% (Fig. 3c). To further quantify the nanoscale heterogeneity, the STEM data were deeply analyzed (Supplementary Figs. S6 and S7). Supplementary Fig. S6a shows an experimental STEM image of WS<sub>0.96</sub>Se<sub>1.04</sub> with a Voronoi pattern overlay. The color overlay displays the distribution of Se + Se (yellow), Se + S (green), and S + S (darker green) sites in the observed image, confirming that S and Se are intermixed at the atomic scale. As additionally shown in Supplementary Fig. S6b, the simulated distribution of Se and S sites based on Monte-Carlo simulation in the case of the maximum tendency of intermixing is comparable to the experimentally measured distribution. Any possible correlation between Se and S sites over a short range was further checked by calculating the relative occupancy for S + S sites and Se + Se sites (Supplementary Fig. S7). We find that there is a slight short-range correlation in which the same chalcogen sites tend to gather with slightly higher probability. For example, for Se occupancy sites, the probability that its nearest neighbor site is occupied by the same Se sites is ~1.8 times higher than that of the S site (Supplementary Fig. S7b, c). Similarly, the nearest neighbor sites of S sites are occupied by S sites 1.8 times more likely compared to Se sites. Correlation behavior functions can be fitted with  $f(x) = Ae^{-x/\tau} + 1$ , where  $A$  is the fitting parameter and  $\tau$  corresponds to a correlation length scale. The observed short-range correlation disappears at ~2 nm (Supplementary Fig. S7c). These results confirmed the substitutional alloying of the WS<sub>2x</sub>Se<sub>2(1-x)</sub> film without any phase separation between WS<sub>2</sub> and WSe<sub>2</sub>.

To verify the atomic binding state of W 4f, S 2p, and Se 3p of WS<sub>2x</sub>Se<sub>2(1-x)</sub> alloys, we conducted X-ray photoelectron

spectroscopy (XPS) using a conventional X-ray source (Al K $\alpha$  radiation), wherein the spectra were obtained by fitting with a Gaussian–Lorentzian function and Shirley backgrounds (Supplementary Fig. S8). With increasing sulfur concentration, the peaks of the W 4f<sub>5/2</sub> and W 4f<sub>7/2</sub> binding energies gradually shifted to higher energies, i.e., from 33.50 to 34.25 eV and 31.38 to 32.13 eV, respectively (Fig. 3d). This phenomenon meant that the binding state of tungsten could be effectively changed by modulating the S/Se ratio because of the difference in the electronegativity of the S and Se atoms, leading to its bond with W atoms. Moreover, the chemical binding states of S 2p and Se 3p were systematically magnified or diminished by changing the S/Se ratio, as shown in Fig. 3e. For quantitative analysis, the accurate atomic concentration (%) of S was calculated using the following equation:

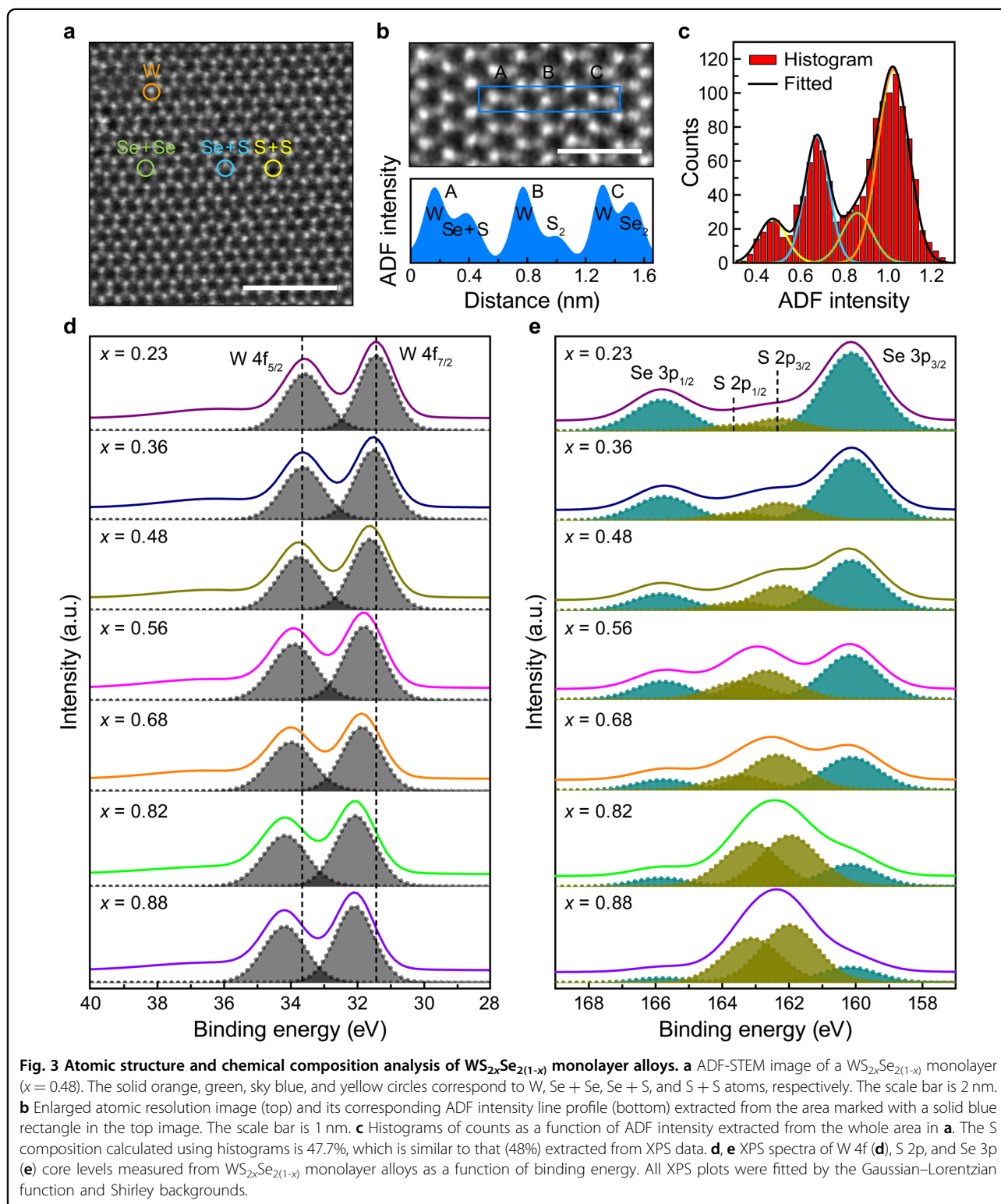
$$C_S = 100 \times \frac{I_S \times F_{Se}}{I_S \times F_{Se} + I_{Se} \times F_S} \quad (1)$$

where  $I_S$  and  $I_{Se}$  are the integrated peak intensities of S 2p<sub>3/2</sub> and Se 3p<sub>3/2</sub>, respectively, and  $F_S$  (0.4453) and  $F_{Se}$  (0.8493) are the relative sensitivity factors for S and Se, respectively<sup>19,38</sup>. From these XPS results, we confirmed that the S compositions varied between 0 and 100%, corresponding to the changing amount of chalcogen precursors during the growth of WS<sub>2x</sub>Se<sub>2(1-x)</sub> alloys (Supplementary Table S2 and Supplementary Fig. S9).

From the TEM and XPS analyses, we examined the relationship between the optical bandgap energies and chalcogen compositions in the WS<sub>2x</sub>Se<sub>2(1-x)</sub> alloys (Supplementary Table S3). To exclude a mixed signal originating from domains with different compositions<sup>39,40</sup>, TEM-EDS analysis with 20-nm resolution was carried out, providing statistical data of sulfur composition for the alloyed samples. The experimentally determined optical bandgap exhibited a nearly linear dependence on the sulfur composition, as shown in Fig. 4a. The optical bandgap energy for ternary semiconductor alloys can be described by the following bowing equation<sup>41</sup>:

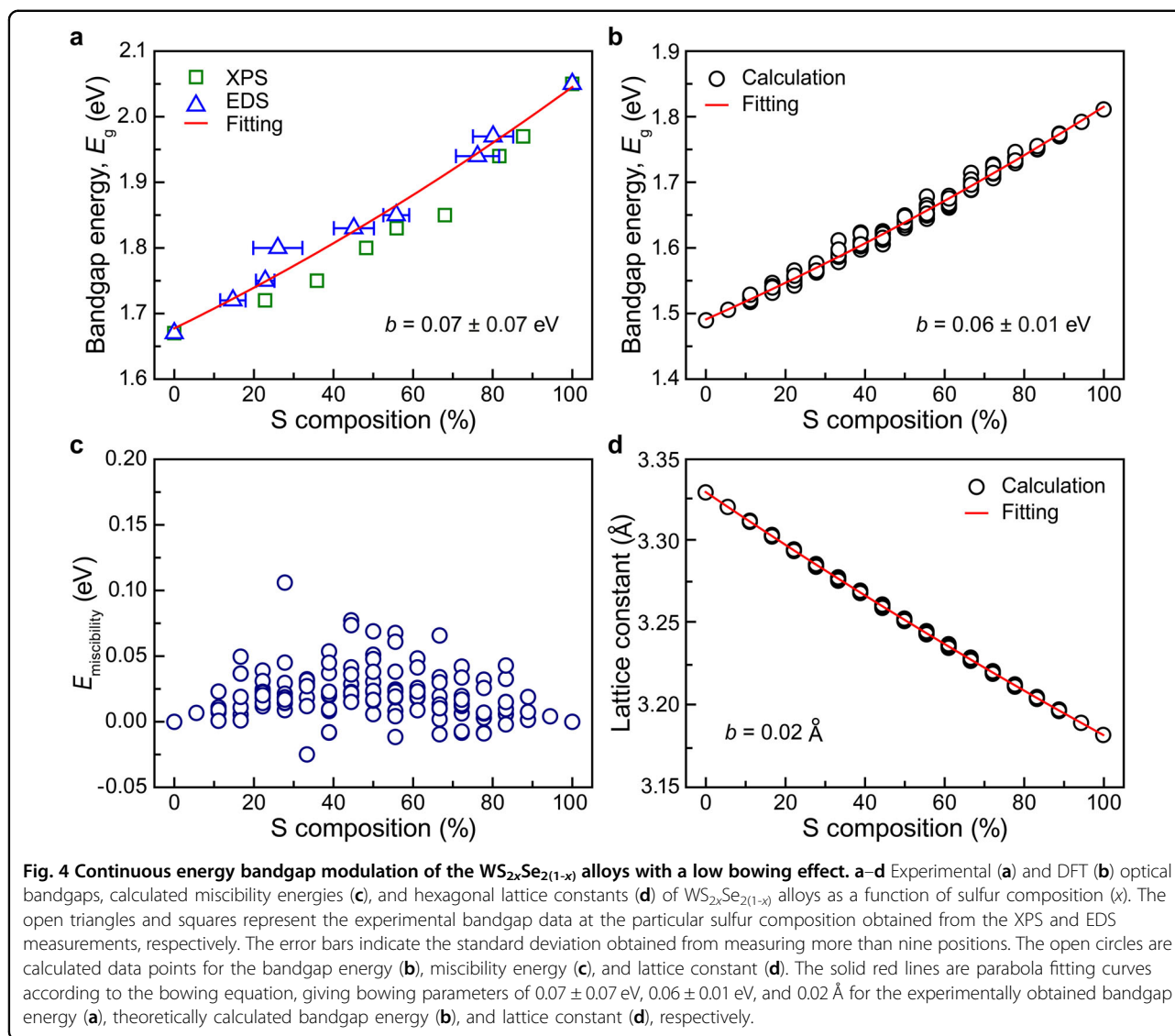
$$E_g(x) = xE_g^{WS_2} + (1-x)E_g^{WSe_2} - bx(1-x) \quad (2)$$

where  $E_g^{WS_2}$  and  $E_g^{WSe_2}$  are the bandgap energies of WS<sub>2</sub> and WSe<sub>2</sub>, respectively, and  $x$  and  $b$  are the sulfur composition and bowing parameter, respectively. The bowing parameter was derived by fitting to Eq. (2) and was determined to be 0.07 ± 0.07 eV. This vanishingly small bowing parameter of MOCVD-grown WS<sub>2(1-x)</sub>Se<sub>2x</sub> alloys coincides well with previous experiments for CVD-grown WS<sub>2(1-x)</sub>Se<sub>2x</sub> and MoS<sub>2(1-x)</sub>Se<sub>2x</sub> alloys<sup>42</sup>. Such a low bowing effect is explained by the fact that the energy bandgap (the conduction-band minimum and valence-band maximum) of TMD monolayers is mainly affected



by the *d*-electron orbitals on transition metal atoms<sup>43</sup>. In addition, the lattice constant of chalcogen alloys tends to increase almost linearly with composition, leading to the linear dependence of bandgap energy. On the other hand,

the transition metal alloys showed relatively large bowing parameters of 0.25 eV for  $Mo_{1-x}W_xS_2$ <sup>43</sup> and 0.15 eV for  $Mo_{1-x}W_xSe_2$ <sup>44</sup> because the competition in constructing the band edges from two different metal atoms causes



pronounced bowing behavior. In addition, note that  $WS_{2(1-x)}Se_{2x}$  alloys exhibit much lower bowing parameters than bulk alloys such as  $GaAs_{1-x}Sb_x$  (1.43 eV)<sup>45</sup> and  $Al_{1-x}Ga_xN$  (0.94 eV)<sup>46</sup> owing to the strain relaxation originating from low dimensionality and the similar electronegativities of 2.58 and 2.55 for S and Se, respectively<sup>6</sup>.

The experimentally confirmed bowing alleviation was further studied by density functional theory (DFT) calculations. Although DFT is known to underestimate the bandgap, it can describe the bandgap changes. As shown in Fig. 4b, the resultant bandgap evolution with alloying showed negligible bandgap bowing (0.06 eV) because of the small distortion energy of  $WS_{2x}Se_{2(1-x)}$ , originating from the nearly same bond lengths as those for W–S and W–Se in the alloys<sup>6,47,48</sup>. The calculated miscibility energies of  $WS_{2x}Se_{2(1-x)}$  alloys are plotted in Fig. 4c as a function of

sulfur composition ( $x$ ). The convex hull showed negative energy, indicating the stable formation of the  $WS_{2x}Se_{2(1-x)}$  alloys without any structural phase transition. Electron localization by the anionic ( $S_{2x}Se_{2(1-x)}$ ) alloying disorder was expected to be small because the band edges were mainly contributed by the cationic W. The optimized hexagonal lattice constants of  $WS_{2x}Se_{2(1-x)}$  are plotted in Fig. 4d as a function of  $x$ . They also exhibited a nearly linear relationship with a small bowing parameter of  $0.02$  Å between those of  $WS_2$  and  $WSe_2$ . These experimental and theoretical results implied that systematic bandgap engineering with full-composition tunability in 2D TMD compounds could be achieved by atomic-scale substitutional alloying without any significant detrimental defects or structural disorders during MOCVD growth.

We further demonstrated the capability of fabricating hetero-multilayers via artificial *vdW* stacking of differently

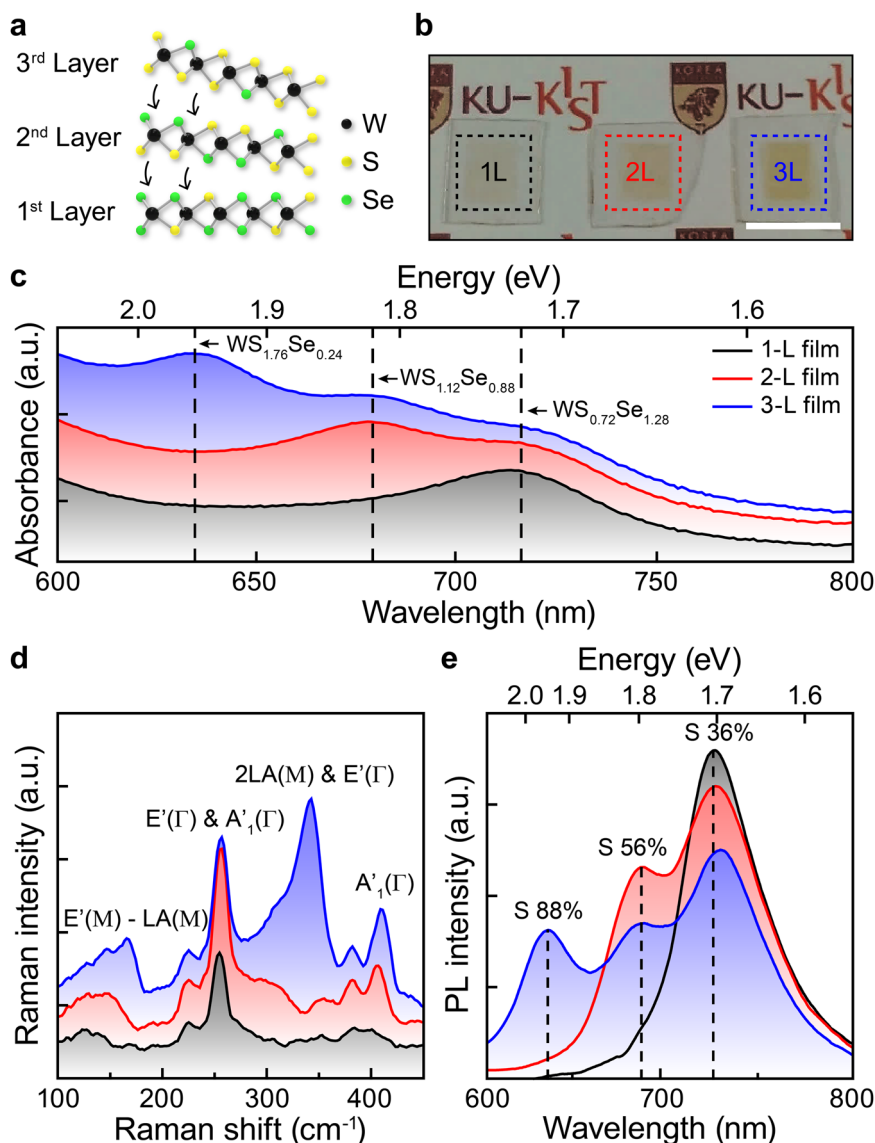


**Fig. 5** Hetero-multilayers of differently alloyed  $WS_{2x}Se_{2(1-x)}$  films via artificial vdW stacking. **a** A schematic of the vertical layer-by-layer assembly of three-layer  $WS_{2x}Se_{2(1-x)}$  heterostructures comprising different S compositions. 1<sup>st</sup> layer:  $WS_{0.72}Se_{1.28}$ , 2<sup>nd</sup> layer:  $WS_{1.12}Se_{0.88}$ , 3<sup>rd</sup> layer:  $WS_{1.76}Se_{0.24}$ . The black, yellow, and green balls represent W, S, and Se atoms, respectively. **b** Photograph of 1-L (left), 2-L (middle), and 3-L (right) films transferred onto sapphire substrates. The scale bar is 1 cm. **c–e** Corresponding UV/Vis absorption (**c**), Raman (**d**), and PL (**e**) spectra of hetero-multilayer  $WS_{2x}Se_{2(1-x)}$  films. The solid black, red, and blue lines correspond to 1-L, 2-L, and 3-L  $WS_{2x}Se_{2(1-x)}$  films, respectively.

alloyed monolayers. Figure 5a shows a schematic of vertically stacked  $WS_{2x}Se_{2(1-x)}$  hetero-multilayers. To fabricate hetero-multilayer films on transparent c-sapphire substrates, we adopted the dry-transfer method, which uses thermal release tape. This process is known to cause less film damage than the wet-etching method, which uses a strong acid (HF) or base (KOH)<sup>23</sup>. Figure 5b shows the optical microscopy images of the  $WS_{2x}Se_{2(1-x)}$  hetero-multilayer films with different S compositions of 36, 56, and 88% (1-L (S 36%), 2-L (S 36 + 56%), and 3-L (S 36 + 56 + 88%) films), fabricated by repeating the transfer

process (see the Methods section for details). As shown in the absorbance spectra (Fig. 5c), the hetero-multilayers exhibited multiple local absorbance maxima originating from exciton resonances in each alloyed film. The absolute light absorption per unit thickness could be further increased by enhancing light–matter interactions with optical structures such as cavities<sup>49</sup>, superlattices<sup>50</sup>, and plasmonic nanostructures<sup>51</sup>. In addition, all the characteristic vibration modes in the Raman spectra of hetero-multilayers (Fig. 5d) appeared as a result of the superposition of vibration modes of the individual layers. These

results indicated that each layer preserved its monolayer characteristics even after stacking. Furthermore, the distinctive exciton peaks in the PL spectra (Fig. 5e) resulted from the constituent layers (728, 689, and 641 nm for  $WS_{0.72}Se_{1.28}$ ,  $WS_{1.12}Se_{0.88}$ , and  $WS_{1.76}Se_{0.24}$ , respectively) that appeared progressively during the stacking of the monolayers. However, due to interlayer charge transfer processes, the PL intensities of the heterostacked film were quenched compared to those of individual films<sup>52</sup>. All the results demonstrated that the fabrication of artificially stacked hetero-multilayers offered an additional route to modulate the optical properties of alloyed TMD films in a controlled manner.

## Conclusion

We demonstrated the wafer-scale growth and systematic bandgap engineering of  $WS_{2x}Se_{2(1-x)}$  monolayer alloys with full-composition tunability by controlling the molar flow rates of vapor-phase precursors using our home-built MOCVD system. Varying the relative ratio of substitutional chalcogen atoms led to the controlled modulation of both chemical composition and optical bandgap, as confirmed by several characterization techniques, including absorbance, PL, Raman, TEM, and XPS measurements. Notably, the experimentally determined bandgap and composition exhibited a nearly linear relationship, indicating a low bowing effect, consistent with the theoretical calculations. Furthermore, we modulated the optical properties of the artificially stacked hetero-multilayers to allow for broader light absorption with multiple exciton resonances compared to that of the individual alloyed monolayers. The wafer-scale growth and bandgap engineering of 2D TMD alloys developed in this study present a viable approach for the functional implementation of various optoelectronics based on 2D semiconductors.

## Acknowledgements

This work was supported by the National Research Foundation (NRF) of Korea grant, funded by the Korean government (MSIT) (2020M3D1A1110548, 2022M3H4A1A01010280, 2017R1A5A1014862 (SRC Program: vdWMRC center), and 2020R1A2C2009389). D.L. acknowledges the support from the NRF of Korea, funded by the Ministry of Education (2020R111A1A01071872) and the Korean government (MSIT) (2021R1C1C2094189).

## Author details

<sup>1</sup>KU-KIST Graduate School of Converging Science and Technology, Korea University, Seoul 02841, Republic of Korea. <sup>2</sup>Department of Physics, Yonsei University, Seoul 03722, Republic of Korea. <sup>3</sup>Korea Research Institute of Standards and Science, Daejeon 34113, Republic of Korea. <sup>4</sup>GRI-TPC International Research Center, Department of Nanotechnology and Advanced Materials Engineering, Sejong University, Seoul 05006, Republic of Korea. <sup>5</sup>School of Physics and Astronomy, University of Manchester, Oxford Road, Manchester M13 9PL, UK. <sup>6</sup>Department of Integrative Energy Engineering, Korea University, Seoul 02841, Republic of Korea. <sup>7</sup>Electronic Materials Research Center, Korea Institute of Science and Technology, Seoul 02792, Republic of Korea

## Author contributions

H.S.K., D.L., and C.-H.L. conceived the idea of the research. H.S.K., J.H.K., and D.H.K. performed the sample fabrication, measurement, and data analysis. S.L., K.L., and K.K. performed TEM measurements. Y.-S.K. performed the density functional theory calculations. H.S.K., Y.J.H., and Y.-J.K. developed techniques for material growth. H.S.K. and D.L. comprehensively analyzed all data and wrote the manuscript. All authors discussed the results and commented on the manuscript. C.-H.L. supervised the project.

## Conflict of interest

The authors declare no competing interests.

## Publisher's note

Springer Nature remains neutral with regard to jurisdictional claims in published maps and institutional affiliations.

**Supplementary information** The online version contains supplementary material available at <https://doi.org/10.1038/s41427-022-00437-w>.

Received: 3 June 2022 Revised: 28 September 2022 Accepted: 5 October 2022.

Published online: 18 November 2022

## References

- Akinwande, D. et al. Graphene and two-dimensional materials for silicon technology. *Nature* **573**, 507–518 (2019).
- Liu, C. et al. Two-dimensional materials for next-generation computing technologies. *Nat. Nanotechnol.* **15**, 545–557 (2020).
- Liu, Y. et al. Promises and prospects of two-dimensional transistors. *Nature* **591**, 43–53 (2021).
- Liu, Y., Stradins, P. & Wei, S.-H. Van der Waals metal-semiconductor junction: weak Fermi level pinning enables effective tuning of Schottky barrier. *Sci. Adv.* **2**, e1600069 (2016).
- Qiu, Q. & Huang, Z. Photodetectors of 2D materials from ultraviolet to terahertz waves. *Adv. Mater.* **33**, 2008126 (2021).
- Chaves, A. et al. Bandgap engineering of two-dimensional semiconductor materials. *npj 2D Mater. Appl.* **4**, 29 (2020).
- Kang, S. et al. 2D semiconducting materials for electronic and optoelectronic applications: potential and challenge. *2D Mater.* **7**, 022003 (2020).
- Kim, Y. S. et al. Atomic-layer-confined multiple quantum wells enabled by monolithic bandgap engineering of transition metal dichalcogenides. *Sci. Adv.* **7**, eabd7921 (2021).
- Li, Z. et al. Efficient strain modulation of 2D materials via polymer encapsulation. *Nat. Commun.* **11**, 1151 (2020).
- Mann, J. et al. 2-Dimensional transition metal dichalcogenides with tunable direct band gaps:  $MoS_{2(1-x)}Se_{2x}$  monolayers. *Adv. Mater.* **26**, 1399–1404 (2014).
- Manzeli, S., Ovchinnikov, D., Pasquier, D., Yazyev, O. V. & Kis, A. 2D transition metal dichalcogenides. *Nat. Rev. Mater.* **2**, 17033 (2017).
- Susarla, S. et al. Quaternary 2D transition metal dichalcogenides (TMDs) with tunable bandgap. *Adv. Mater.* **29**, 1702457 (2017).
- Ning, C.-Z., Dou, L. & Yang, P. Bandgap engineering in semiconductor alloy nanomaterials with widely tunable compositions. *Nat. Rev. Mater.* **2**, 17070 (2017).
- Capasso, F. Band-gap engineering: from physics and materials to new semiconductor devices. *Science* **235**, 172–176 (1987).
- Chen, R. et al. Nanolasers grown on silicon. *Nat. Photonics* **5**, 170–175 (2011).
- Assefa, S., Xia, F. & Vlasov, Y. A. Reinventing germanium avalanche photodetector for nanophotonic on-chip optical interconnects. *Nature* **464**, 80–84 (2010).
- Hirschman, K. D., Tsybeskov, L., Dutttagupta, S. P. & Fauchet, P. M. Silicon-based visible light-emitting devices integrated into microelectronic circuits. *Nature* **384**, 338–341 (1996).
- George, E. P., Raabe, D. & Ritchie, R. O. High-entropy alloys. *Nat. Rev. Mater.* **4**, 515–534 (2019).
- Lim, Y. R. et al. Atomic-level customization of 4 in. Transition metal dichalcogenide multilayer alloys for industrial applications. *Adv. Mater.* **31**, 1901405 (2019).
- Song, J.-G. et al. Controllable synthesis of molybdenum tungsten disulfide alloy for vertically composition-controlled multilayer. *Nat. Commun.* **6**, 7817 (2015).

21. Fu, Q. et al. Synthesis and enhanced electrochemical catalytic performance of monolayer  $WS_{2(1-x)}Se_{2x}$  with a tunable band gap. *Adv. Mater.* **27**, 4732–4738 (2015).
22. Kang, K. et al. High-mobility three-atom-thick semiconducting films with wafer-scale homogeneity. *Nature* **520**, 656–660 (2015).
23. Kang, K. et al. Layer-by-layer assembly of two-dimensional materials into wafer-scale heterostructures. *Nature* **550**, 229–233 (2017).
24. Kim, S.-Y., Kwak, J., Ciobanu, C. V. & Kwon, S.-Y. Recent developments in controlled vapor-phase growth of 2D group 6 transition metal dichalcogenides. *Adv. Mater.* **31**, 1804939 (2019).
25. Jin, G. et al. Heteroepitaxial van der Waals semiconductor superlattices. *Nat. Nanotechnol.* **16**, 1092–1098 (2021).
26. Kresse, G. & Furthmüller, J. Efficient iterative schemes for ab initio total-energy calculations using a plane-wave basis set. *Phys. Rev. B* **54**, 11169–11186 (1996).
27. Kresse, G. & Joubert, D. From ultrasoft pseudopotentials to the projector augmented-wave method. *Phys. Rev. B* **59**, 1758–1775 (1999).
28. Blöchl, P. E. Projector augmented-wave method. *Phys. Rev. B* **50**, 17953–17979 (1994).
29. Perdew, J. P., Burke, K. & Ernzerhof, M. Generalized gradient approximation made simple. *Phys. Rev. Lett.* **77**, 3865–3868 (1996).
30. Grimme, S., Antony, J., Ehrlich, S. & Krieg, H. A consistent and accurate ab initio parametrization of density functional dispersion correction (DFT-D) for the 94 elements H–Pu. *J. Chem. Phys.* **132**, 154104 (2010).
31. Grimme, S., Ehrlich, S. & Goerigk, L. Effect of the damping function in dispersion corrected density functional theory. *J. Comput. Chem.* **32**, 1456–1465 (2011).
32. Palumbo, M., Bernardi, M. & Grossman, J. C. Exciton radiative lifetimes in two-dimensional transition metal dichalcogenides. *Nano Lett.* **15**, 2794–2800 (2015).
33. Zhang, X. et al. Phonon and Raman scattering of two-dimensional transition metal dichalcogenides from monolayer, multilayer to bulk material. *Chem. Soc. Rev.* **44**, 2757–2785 (2015).
34. Duan, X. et al. Synthesis of  $WS_{2x}Se_{2-2x}$  alloy nanosheets with composition-tunable electronic properties. *Nano Lett.* **16**, 264–269 (2016).
35. Biswas, S. et al. Non-equilibrium induction of tin in germanium: towards direct bandgap  $Ge_{1-x}Sn_x$  nanowires. *Nat. Commun.* **7**, 11405 (2016).
36. Sriv, T. et al. Optical phonons of  $SnSe_{(1-x)}S_x$  layered semiconductor alloys. *Sci. Rep.* **10**, 11761 (2020).
37. Cohen, A. et al. Growth-etch metal–organic chemical vapor deposition approach of  $WS_2$  atomic layers. *ACS Nano* **15**, 526–538 (2021).
38. Kiran, V., Mukherjee, D., Jenjeti, R. N. & Sampath, S. Active guests in the  $MoS_2/MoSe_2$  host lattice: efficient hydrogen evolution using few-layer alloys of  $MoS_{2(1-x)}Se_{2x}$ . *Nanoscale* **6**, 12856–12863 (2014).
39. Jo, K. et al. Direct optoelectronic imaging of 2D semiconductor–3D metal buried interfaces. *ACS Nano* **15**, 5618–5630 (2021).
40. Moore, D. et al. Uncovering topographically hidden features in 2D  $MoSe_2$  with correlated potential and optical nanoprobe. *npj 2D Mater. Appl.* **4**, 44 (2020).
41. Wei, S.-H. & Zunger, A. Giant and composition-dependent optical bowing coefficient in GaAsN alloys. *Phys. Rev. Lett.* **76**, 664–667 (1996).
42. Li, H. et al. Growth of alloy  $MoS_{2x}Se_{2(1-x)}$  nanosheets with fully tunable chemical compositions and optical properties. *J. Am. Chem. Soc.* **136**, 3756–3759 (2014).
43. Chen, Y. et al. Tunable band gap photoluminescence from atomically thin transition-metal dichalcogenide alloys. *ACS Nano* **7**, 4610–4616 (2013).
44. Zhang, M. et al. Two-dimensional molybdenum tungsten diselenide alloys: photoluminescence, Raman scattering, and electrical transport. *ACS Nano* **8**, 7130–7137 (2014).
45. Kopaček, J. et al. Experimental and theoretical studies of the electronic band structure of bulk and atomically thin  $Mo_{1-x}W_xSe_2$  alloys. *ACS Omega* **6**, 19893–19900 (2021).
46. Coughlan, C., Schulz, S., Caro, M. A. & O'Reilly, E. P. Band gap bowing and optical polarization switching in AlGaIn alloys. *Phys. Status Solidi B* **252**, 879–884 (2015).
47. Dong, J., Zhao, Y. & Ouyang, G. The effect of alloying on the band engineering of two-dimensional transition metal dichalcogenides. *Phys. E Low-Dimens. Syst. Nanostruct.* **105**, 90–96 (2019).
48. Kang, J., Tongay, S., Li, J. & Wu, J. Monolayer semiconducting transition metal dichalcogenide alloys: stability and band bowing. *J. Appl. Phys.* **113**, 143703 (2013).
49. Epstein, I. et al. Near-unity light absorption in a monolayer  $WS_2$  Van der Waals heterostructure cavity. *Nano Lett.* **20**, 3545–3552 (2020).
50. Kumar, P. et al. Light–matter coupling in large-area van der Waals superlattices. *Nat. Nanotechnol.* **17**, 182–189 (2022).
51. Zhang, H. et al. Hybrid exciton-plasmon-polaritons in van der Waals semiconductor gratings. *Nat. Commun.* **11**, 3552 (2020).
52. Lee, C.-H. et al. Atomically thin p–n junctions with van der Waals hetero-interfaces. *Nat. Nanotechnol.* **9**, 676–681 (2014).